Low-Power/High-Gain Flexible Complementary Circuits Based on Printed Organic Electrochemical Transistors

Downloaded from: https://research.chalmers.se, 2026-10-12 18:48 UTC

Citation for the original published paper (version of record):

Yang, C., Tu, D., Ruoko, T. et al (2022). Low-Power/High-Gain Flexible Complementary Circuits Based on Printed Organic Electrochemical
Transistors. Advanced Electronic Materials, 8(3). http://dx.doi.org/10.1002/aelm.202100907

N.B. When citing this work, cite the original published paper.

research.chalmers.se offers the possibility of retrieving research publications produced at Chalmers University of Technology. It covers all kind of research output: articles, dissertations, conference papers, reports etc. since 2004. research.chalmers.se is administrated and maintained by Chalmers Library

(article starts on next page)

Check for updates

ADVANCED ELECTRONIC MATERIALS
www.advelectronicmat.de

Low-Power/High-Gain Flexible Complementary Circuits Based on Printed Organic Electrochemical Transistors

*Chi-Yuan Yang, Deyu Tu, Tero-Petri Ruoko, Jennifer Y. Gerasimov, Han-Yan Wu, Padinhare Cholakkal Harikesh, Matteo Massetti, Marc-Antoine Stoeckel, Renee Kroon, Christian Müller, Magnus Berggren, and Simone Fabiano**

The ability to accurately extract low-amplitude voltage signals is crucial in several fields, ranging from single-use diagnostics and medical technology to robotics and the Internet of Things (IoT). The organic electrochemical transistor (OECT), which features large transconductance values at low operating voltages, is ideal for monitoring small signals. Here, low-power and high-gain flexible circuits based on printed complementary OECTs are reported. This work leverages the low threshold voltage of both p-type and n-type enhancement-mode OECTs to develop complementary voltage amplifiers that can sense voltages as low as 100 μV, with gains of 30.4 dB and at a power consumption of 0.1–2.7 μW (single-stage amplifier). At the optimal operating conditions, the voltage gain normalized to power consumption reaches 169 dB μW^{-1}, which is >50 times larger than state-of-the-art OECT-based amplifiers. In a monolithically integrated two-stage configuration, these complementary voltage amplifiers reach voltage gains of 193 V/V, which are among the highest for emerging complementary metal-oxide-semiconductor-like technologies operating at supply voltages below 1 V. These flexible complementary circuits based on printed OECTs define a new power-efficient platform for sensing and amplifying low-amplitude voltage signals in several emerging beyond-silicon applications.

1. Introduction

Complementary metal-oxide-semiconductor (CMOS) field-effect transistors, made from silicon (Si), have been the workhorse of the integrated circuit (IC) industry since the 1980s, in part due to their low power consumption. Dennard scaling,[1] the CMOS scaling law, states that the supply voltage for each new CMOS generation is reduced by 30%, and the power consumption subsequentially reduces by 50%. After decades of development, the latest 7-nm-node CMOS process reaches a supply voltage of 0.75 V.[2]

Today, the Si-CMOS technology is heavily explored in Internet of Things (IoT) applications, serving as low-power outposts that record physical sensor parameters (e.g., motion, light, temperature), communicate over long distances, and harvest and store energy for its operation.[3] Expanding IoT modules with flexible, soft, or large-area chemical sensors and actuators only possible off-Si, enables a circuit technology that can amplify and route signals, facilitating signal compatibility and low-cost integration between Si-technology and embedded devices. Further, for many IoT and bioelectronic applications (e.g., (bio-)chemical sensors and neuronal interfacing), the on-site technology is preferably realized without Si-chips to enable many different form factors, proximity, elasticity, and signal transduction, tailor-made for the actual chemical/biological environment. Also in this case, a low-power/voltage, high-performing, and flexible circuit technology operating at the site of stimulation or sensing is needed to record and transfer signals at high signal-to-noise performance.

C.-Y. Yang, D. Tu, T.-P. Ruoko, J. Y. Gerasimov, H.-Y. Wu, P. C. Harikesh, M. Massetti, M.-A. Stoeckel, R. Kroon, M. Berggren, S. Fabiano
Laboratory of Organic Electronics
Department of Science and Technology
Linköping University
Norrköping SE-601 74, Sweden
E-mail: simone.fabiano@liu.se

The ORCID identification number(s) for the author(s) of this article can be found under https://doi.org/10.1002/aelm.202100907.

© 2021 The Authors. Advanced Electronic Materials published by Wiley-VCH GmbH. This is an open access article under the terms of the Creative Commons Attribution License, which permits use, distribution and reproduction in any medium, provided the original work is properly cited.

DOI: 10.1002/aelm.202100907

H.-Y. Wu, R. Kroon, M. Berggren, S. Fabiano
Wallenberg Wood Science Center
Department of Science and Technology
Linköping University
Norrköping SE-601 74, Sweden

C. Müller
Wallenberg Wood Science Center
Department of Chemistry and Chemical Engineering
Chalmers University of Technology
Göteborg SE-412 06, Sweden

M. Berggren, S. Fabiano
n-Ink AB
Teknikringen 7, Linköping SE-583 30, Sweden

 © 2021 The Authors. Advanced Electronic Materials published by Wiley-VCH GmbH

Unlike field-effect transistors, organic electrochemical transistors (OECTs) typically operate at less than 1 V and consist of a mixed ionic-electronic conducting polymer channel[4,5] and a gate connected by a common electrolyte.[6] When a voltage is applied to the gate, ions from the electrolyte enter the bulk of the channel material to compensate for the injected charge carriers in the oxidized or reduced organic semiconductor, thus modulating the channel conductance. Since OECTs operate at low voltages and exhibit transconductance values that are orders of magnitude higher than their (organic) field-effect transistor counterparts, they are ideally suited to sense and amplify low-amplitude voltage signals.[7] To date, OECTs have been used to construct digital circuits,[8–11] sensors of biological, physical, and chemical signals,[12–14] and neuromorphic computing devices.[15–19]

While the large OECT transconductance can translate a small voltage into a sizable current, post-signal processing often necessitates further current-to-voltage conversion. To address this need, a handful of high-gain OECT-based voltage amplifiers have been developed.[20–26] For instance, Braendlein et al. reported a voltage amplifier that consists of a depletion-mode OECT based on the hole-transporting (p-type) polymer poly(3,4-ethylenedioxythiophene):poly(styrenesulfonate) (PEDOT:PSS) and a resistor load to record electrocardiogram signals,[22] while Romele et al. demonstrated voltage gains over 100 using crystallized PEDOT:PSS-based OECTs.[24] However, amplifiers based on depletion-mode OECTs almost universally suffer from high power consumption, in some instances reaching values as high as 1350 μW.[22] Borrowing from thin-film transistors,[27,28] Rivnay et al. were recently able to reduce the power consumption of enhancement-mode OECT-based amplifiers operated in the subthreshold regime down to 20 μW, although at the expense of the voltage gain (≈9.3 V/V).[23]

Recently, we reported a different approach to reducing power consumption by developing the first complementary OECT-based inverters,[26] which takes inspiration from the CMOS technology. Si-based electronics have shown significant improvements in power efficiency afforded by CMOS circuits compared to unipolar technologies, wherein only one type of transistor is used.[29] Romele et al. expanded on our results and developed complementary OECTs comprising BBL as the n-type transistor and PEDOT:PSS as the p-type transistor.[25] However, both of these examples of CMOS-like OECT-based inverters showed power consumption >10 μW at V_{DD} = 0.5 V, and were based on photolithography-made devices incorporating liquid electrolytes, which hamper their large-scale, solid-state integration. To this end, printing technologies, such as ink-jet printing, screen-printing, aerosol-jet printing, and spray-coating, can enable flexibility, conformability, large-scale integration, and cost-efficiency.[10,30] However, despite prior reports of large-scale circuits based on all-printed unipolar OECTs[8] and photolithography-made complementary OECTs,[25,26] printed solid-state complementary OECTs and circuits have not yet been reported.

Here, we report printed and flexible circuits based on complementary OECTs, which operate at low voltages (0.3–0.7 V) with a static power consumption of 12 nW and a dynamic power consumption as low as 0.1 μW per switch. This power consumption level is at least two orders of magnitude lower than state-of-the-art complementary OECTs. Both p-type and n-type OECTs, with planarly integrated gates, operate in the enhancement-mode, with maximum transconductance of ≈0.20 mS and threshold voltages of less than |0.25| V, which enables low voltage operation. To facilitate solid-state integration, we developed printable polycationic (for p-type OECTs) and polyanionic (for n-type OECTs) hydrogels that show good ion mobility, enabling faster OECT response (16–160 ms) than previously reported photolithography-made complementary OECTs.[25,26] Electrochemical bulk doping of the channel materials is confirmed by in situ spectroelectrochemistry measurements. The driving strength and the operating voltage of both p-type and n-type OECTs are well balanced and enable the development of single-stage complementary inverters having voltage gains of up to 26 V/V and excellent noise margin (89%). With a DC offset at the input, the inverter operates as a push-pull amplifier which is able to sense AC voltage signals as low as 100 μV and a maximum gain of 30.4 dB. This ability to detect small voltage signals with very low power consumption yields a power-normalized gain of up to 169 dB μW^{-1}, which is over 50 times greater than state-of-the-art amplifiers based on OECT technologies. Because of the planarly integrated gates and well-matched operating points, we were able to demonstrate monolithically integrated two-stage amplifiers showing a record-high DC gain of 193 V/V, which is the highest gain among emerging CMOS-like thin-films technologies operating at sub-1-V regime to date. In addition, the successful implementation of 10 complementary OECTs into a five-stage ring oscillator shows potential for large-scale integration. Our inverters and voltage amplifiers based on printed complementary OECTs offer a power-efficient solution for autonomous, conformable, wearable, and portable sensors consisting of both digital and analog circuits. In addition, the low operation voltage (0.3 V) offers the possibility of being (self-)powered by light, heat, wireless power, triboelectricity, and other power sources that can only provide low voltage and/or limited power supply, thus opening the way to battery-free wearable electronics.

2. Results and Discussion

2.1. Printed Complementary Organic Electrochemical Transistors

Complementary electronic circuitries require the development of both p-type and n-type enhancement-mode OECTs. Here, we use polythiophene functionalized with tetraethylene glycol side chains (P($g_4$2T-T)) and poly(benzimidazobenzophenanthroline) (BBL) as the p-type and n-type semiconducting polymers, respectively (**Figure 1**a). While neither P($g_4$2T-T) nor BBL are soluble in water/alcohols, they can be dispersed in alcohol solvents in the form of nanoparticle inks, which are better suited for large-scale printing. The BBL nanoparticles are obtained by solvent exchange from BBL-methanesulfonic acid (MSA) solution to isopropanol (IPA) under rapid stirring, whereas the P($g_4$2T-T) nanoparticles can be obtained by solvent exchange from its chloroform solution to IPA. The nanoparticle sizes of BBL and P($g_4$2T-T) are 28 and 21 nm, respectively, as measured by dynamic light scattering (DLS, Figure S1, Supporting Information). The BBL and P($g_4$2T-T) nanoparticle dispersion inks in IPA are printable by means of several additive manufacturing techniques, including screen printing, aerosol-jet printing, inkjet printing, and spray-coating. In this manuscript we focus on the later for the deposition of the channel material.

© 2021 The Authors. Advanced Electronic Materials published by Wiley-VCH GmbH

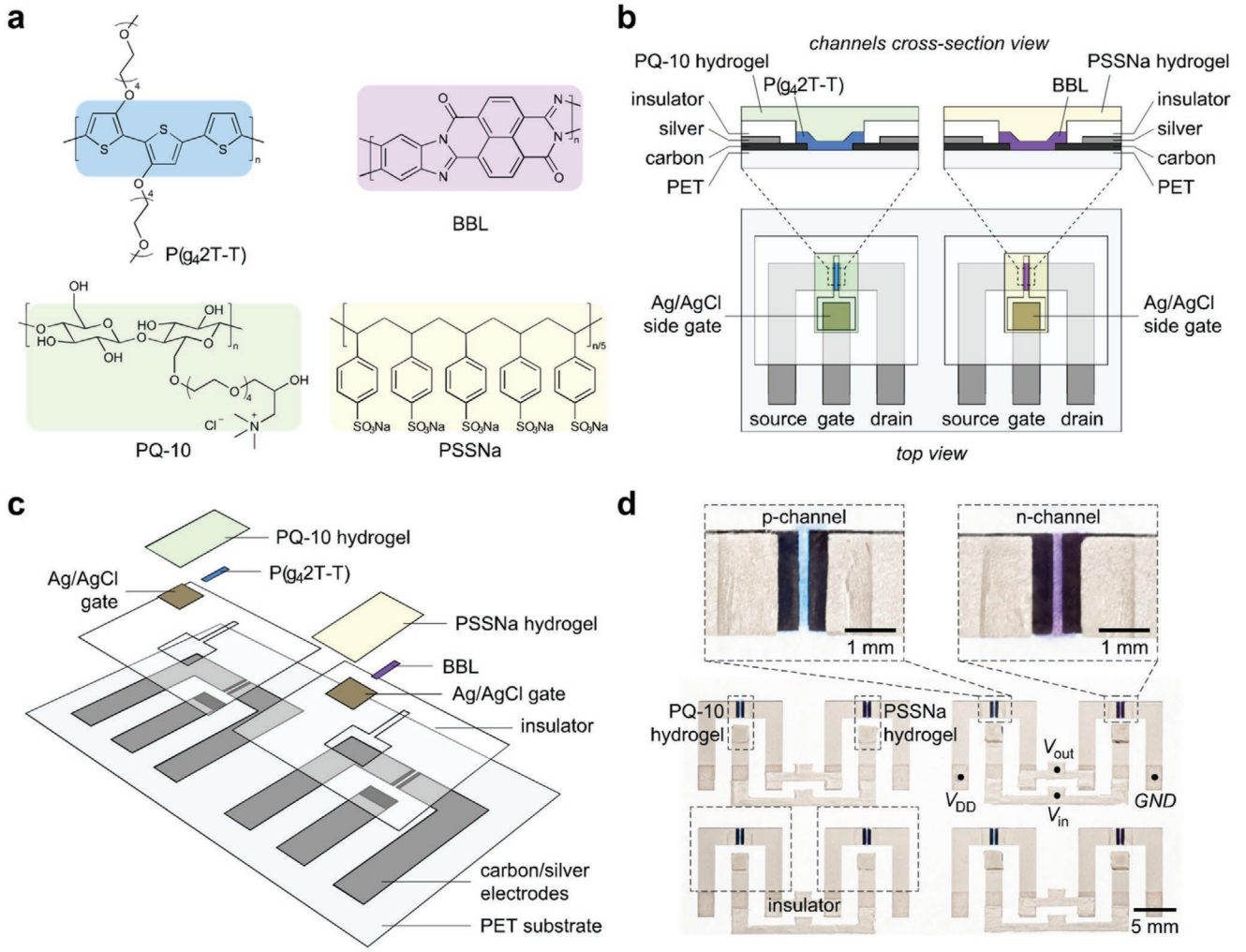

Figure 1. a) Molecular structures of p-type polymer P($g_4$2T-T) and n-type polymer BBL and their corresponding electrolytes, PQ-10 and poly(sodium-4-styrene sulfonate) (PSSNa). b) Illustrated structure of the complementary organic electrochemical transistors (OECTs, cross-section view and top view). c) Breakdown of each layer in the fabrication process of the complementary OECTs. d) Photograph of the as-manufactured complementary OECTs on polyethylene terephthalate (PET) substrate.

To electrostatically gate the P($g_4$2T-T)-based and BBL-based OECTs and to enable solid-state integration, we developed two printable polyanionic and polycationic hydrogels. We chose a poly(sodium-4-styrene sulfonate) (PSSNa, Figure 1a) based hydrogel as the printable sodium electrolyte for the n-channel OECT. D-sorbitol and glycerin are employed to enhance sodium conductivity and the stability of the PSSNa-based hydrogel. We chose polyquaternium-10 (PQ-10, a nontoxic quaternized hydroxyethyl cellulose chloride, Figure 1a) based hydrogel as the printable chloride electrolyte for the p-channel OECT. Both PQ-10 and PSSNa hydrogels have similar or even higher ion conductivity than 0.1 M NaCl aqueous solution (Figure S2, Supporting Information). The all-printed OECT-based circuits are fabricated through the combination of screen-printing and spray-coating (Figure 1b, and Figure S3a, Supporting Information). First, carbon electrode and silver electrode layers are screen printed sequentially on a flexible A3 sized polyethylene terephthalate (PET) substrate (Figure S3b, Supporting Information). We developed OECTs with planarly integrated gates, which enable monolithic integration of complementary OECTs, for the first time. The side-gate configuration, which is optimal for low-cost and large-scale manufacturing, requires fewer processing steps compared to top-gate configurations used in the all-printed unipolar PEDOT:PSS OECTs.[8] The electrochemically inert carbon electrodes are in direct contact with the polymer semiconductor, while the silver underlayer reduces the electrode resistance. The root-mean-square surface roughness of the carbon electrodes is 82.4 nm (Figure S3c,d, Supporting Information). An insulating layer is used to pattern the channel and gate regions.[8] The silver/silver chloride (Ag/AgCl, 100 nm thick) gate layer and polymer semiconductor layer (20 nm for P($g_4$2T-T) and 250 nm for BBL, to match their ON-state channel conductance) are sequentially deposited by spray-coating. The root-mean-square surface roughness of the P($g_4$2T-T) and BBL layers are 5.7 and 12.9 nm, respectively (Figure S3e,f, Supporting Information). Finally, the polymer hydrogel electrolytes (PQ-10 or PSSNa) are screen printed to finish the fabrication of the electrochemical circuits (Figure 1c). For each OECT, the channel length/width (L/W) is 200 μm/2 mm, and the Ag/AgCl gate region is 2 × 2 mm^2.

© 2021 The Authors. Advanced Electronic Materials published by Wiley-VCH GmbH

When implemented as OECT channels, both P($g_4$2T-T) and BBL show relatively low threshold voltages,[31,32] ensuring that a low supply voltage is required for operation. The device structure of the printed complementary OECTs is depicted in Figure 1b–d. More details of device fabrication can be found in the Experimental Section.

2.2. Electrical Characteristics of Printed p-/n-Type OECTs

In a three-terminal (drain, source, and gate) OECT device (Figure 1b), a bias voltage between gate and source (V_{GS}) drives ions from the electrolyte into the channel and results in the modulation of the conductivity between drain and source. For enhancement-mode OECTs, the drain-to-source current (I_{DS}) under a voltage bias (V_{DS}) can be approximately expressed as:[7]

$$I_{DS} = \mu C_V \frac{Wd}{L}\left[(V_{GS} - V_T)V_{DS} - \frac{V_{DS}^2}{2}\right] \quad \text{(linear region)} \tag{1}$$

$$I_{DS} = \mu C_V \frac{Wd}{2L}(V_{GS} - V_T)^2 \quad \text{(saturation region)} \tag{2}$$

where μ is the charge carrier mobility, C_V is the volumetric capacitance, W, L, and d are the channel width, length, and thickness, respectively, and V_T is the threshold voltage. Unlike conventional field-effect transistors, the channel thickness d contributes to the conductivity as the accumulation of charges occurs throughout the entire bulk of the semiconductor layer.

For printed P($g_4$2T-T) OECTs, the application of a negative V_{GS} oxidizes the semiconductor channel and enables the accumulation and transport of holes in the channel under a negative V_{DS}. **Figure 2**a,b shows the typical output ($I_{DS} - V_{DS}$) and transfer ($I_{DS} - V_{GS}$) characteristics of P($g_4$2T-T)-based OECTs reaching an ON/OFF ratio of ≈10^3 at $V_{GS} < 1$ V. The device-to-device variation of the ON-current is found to be 4% (average ON-current value is –49.9 ± 2.0 µA at $V_{GS} = V_{DS} = -0.7$ V for 10 OECTs, Figure S4, Supporting Information). In addition, a negligible hysteresis in I_{DS} is observed over the entire V_{GS} range (Figure 2b), which is beneficial for the stable operation of analog circuits (e.g., amplifiers). The transconductance $g_m = \partial I_{DS}/\partial V_{GS}$, a key figure of merit used to evaluate OECTs, is also shown in Figure 2b. The maximal transconductance of P($g_4$2T-T) OECTs is ≈0.17 mS. From the transfer characteristics in the saturation region, a typical V_T of –0.22 V is extracted (Figure S5a, Supporting Information). From Equation (2) we can then extract the product of mobility and volumetric capacitance $\mu C_V = 22.9$ F cm^{-1} V^{-1} s^{-1} in the saturation region (for V_{DS} between –0.4 and –0.7 V). Furthermore, P($g_4$2T-T)-based OECTs show a maximum intrinsic gain ($A_i = g_m \times r_o$, with r_0 the output resistance $\partial V_{DS}/\partial I_{DS}$) of 62, as reported in Figure S6 (Supporting Information). To further investigate the transient behavior of the P($g_4$2T-T)-based OECTs, a transient I_{DS} was measured when a V_{GS} pulse of –0.7 V was applied at a fixed $V_{DS} = -0.7$ V, as shown in Figure 2c. The P($g_4$2T-T)-based OECTs exhibit relatively fast switching characteristics with a τ_{on}

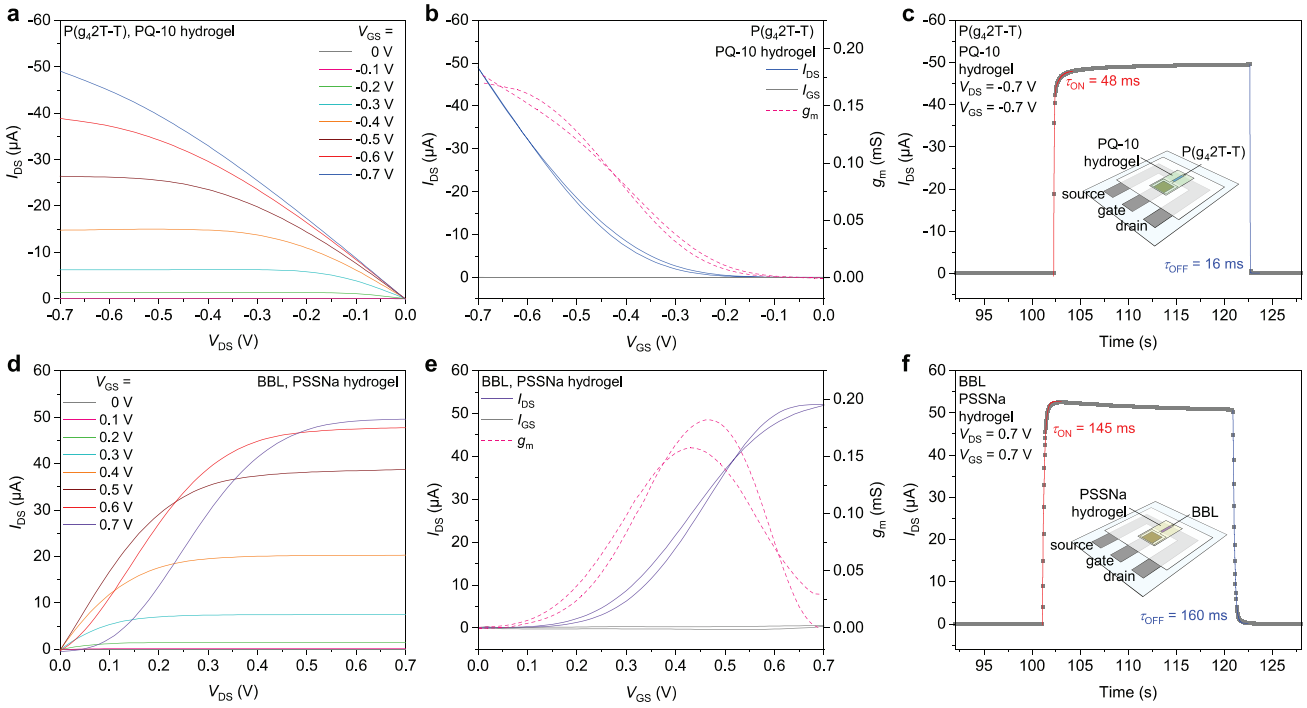

Figure 2. a) Typical output characteristic of printed P($g_4$2T-T) organic electrochemical transistors (OECTs). b) Transfer characteristics and transconductance in saturation region at $V_{DS} = -0.7$ V. c) Switching characteristics of printed P($g_4$2T-T) OECTs, showing a τ_{on} of 48 ms and a τ_{off} of 16 ms. The dimensions of the OECT channel are $W = 2000$ µm, $L = 200$ µm, and $d = 20$ nm. d) Typical output characteristic of printed BBL OECTs. e) Transfer characteristics and transconductance in saturation region at $V_{DS} = -0.7$ V. f) Switching characteristics of printed BBL OECTs, showing a τ_{on} of 145 ms and a τ_{off} of 160 ms. The dimensions of the OECT channel are $W = 2000$ µm, $L = 200$ µm, and $d = 250$ nm.

© 2021 The Authors. Advanced Electronic Materials published by Wiley-VCH GmbH

of 48 ms and a τ_{off} of 16 ms while the rise time (t_r) is 280 ms and the fall time (t_f) is 58 ms (Figure S7a, Supporting Information). For comparison, P($g_4$2T-T)-based OECTs fabricated using the same printed electrodes but with an aqueous electrolyte (0.1 M NaCl) show an almost identical behavior to P($g_4$2T-T)-based OECTs with printed PQ-10 electrolyte (Figures S5b, S7b, S8a-c, Supporting Information). This indicates that the PQ-10 hydrogel enables the development of printable solid-state P($g_4$2T-T) OECTs without compromising the device performance.

Robust operation of CMOS-like inverters requires a balance between the driving strengths of the p-type and n-type transistors to maximize noise margins. For instance, the channel width of the PMOS (p-type MOS) transistor in a Si CMOS inverter is typically advisable to be three times larger than that of the NMOS (n-type MOS) transistor to achieve balanced driving strengths. Because of the volumetric bulk conductivity in OECTs, we are able to achieve a well-balanced p-/n-type OECT operation by using the same channel W and L, but different p-/n-type semiconductor film thickness, so that the same transistor footprint design can be applied regardless of the difference in electron/hole mobility. This OECT feature has no equivalent in other organic and/or inorganic FET technologies, and simplifies substantially the device manufacturing protocol. Figure 2d-f presents the typical electrical characteristics of a printed BBL-based OECT, the characteristics of which were adjusted to match those of the printed P($g_4$2T-T) OECTs in driving strength and operational voltage. As n-type enhancement-mode transistors, a positive voltage on the gate (V_{GS}) turns on the channel conduction by transporting electrons from source to drain under a positive V_{DS}. The ON/OFF current ratio of the printed BBL-based OECTs is typically $\approx 2 \times 10^3$ and the maximal transconductance is 0.18 mS, as shown in Figure 2e. It should be noted that the transconductance reaches its maximum at V_{GS} between 0.4 and 0.5 V, rather than at the highest applied V_{GS} = 0.7 V. This suggests that the printed BBL OECTs are optimally operated at V_{GS} between 0.4 and 0.5 V for applications where high transconductance is desirable (e.g., amplifiers). For these printed BBL OECTs, the device-to-device variation of the ON-current is found to be 3.6% (average ON-current value is 50.4 ± 1.8 μA at $V_{GS} = V_{DS}$ = 0.7 V for 10 OECTs, Figure S4b, Supporting Information). The threshold voltage of the printed BBL-based OECTs is 0.16 V (Figure S5, Supporting Information), as extracted from the transfer curve in the saturation region (Figure 2e). Similarly, the μC_V of the printed BBL OECTs is calculated to be 2.63 F cm^{-1} V^{-1} s^{-1}, using Equation (2). A maximum intrinsic gain A_i of 63 is shown in Figure S6 (Supporting Information). Figure 2f shows the switching characteristics of the printed BBL OECTs with a τ_{on} of 145 ms and a τ_{off} of 160 ms. The corresponding t_r and t_f are 390 and 360 ms, respectively (Figure S7c, Supporting Information). For comparison, BBL-based OECTs with a 0.1 M NaCl aqueous electrolyte show similar characteristics (Figures S5d, S7d, S8d-f, Supporting Information). However, the maximum transconductance of BBL-based OECTs with NaCl electrolyte is shifted to slightly larger V_{GS} = 0.6 V, suggesting that printed BBL OECTs with PSSNa hydrogel are more favorably operated at lower voltages. Both printed P($g_4$2T-T) and BBL OECTs show faster response than similar photolithography-made complementary OECTs,[25,26] with at least one order of magnitude improvement in the transient characteristics.

2.3. In Situ Spectroelectrochemistry of OECTs

To understand the operation of P($g_4$2T-T) and BBL OECTs, we measured absorption spectra of the polymer films on FTO inside a three-electrode electrochemical cell. We used 0.1 M NaCl as the electrolyte and an Ag/AgCl reference electrode to match the OECT characterization. The absorption spectra of the pristine polymers in air are presented in Figure S9 (Supporting Information). Pristine P(g42T-T) films have an absorption maximum at 600 nm followed by a broad polaronic absorption extending into the IR range due to oxygen doping of P($g_4$2T-T) in air.[33] Pristine BBL on the other hand has an absorption maximum at 570 nm with no visible IR tail due to its undoped state. For spectroelectrochemical measurements, the polymers were first fully dedoped by applying V_{GS} = 0.5 V for P($g_4$2T-T) and V_{GS} = −0.7 V for BBL, followed by measuring the baseline. The application of negative gate voltages for P($g_4$2T-T) and positive gate voltages for BBL results in the injection of charges into the polymer layer, compensated by ion diffusion from the electrolyte. The differential absorption spectra from the undoped state during the cyclic voltammetry (CV) scans are presented in **Figure 3**a-c for P(g42T-T) and in Figure 3d-f for BBL. The formation of polarons is clearly seen in the absorption spectra as a bleaching of the ground state absorption band and an accompanying formation of polaronic absorption for both polymers.

For P($g_4$2T-T) the bleaching of the ground state is especially notable, as the extent of the bleaching is larger in magnitude than the ground state absorption of the same sample measured in air. It is important to note that since P($g_4$2T-T) is doped in air, the undoped baseline in the spectroelectrochemistry measurements has a larger ground state absorption. Nevertheless, most of the P($g_4$2T-T) ground state absorption is bleached, illustrating that a majority of P($g_4$2T-T) segments are doped at the highest applied voltages. The bleaching is accompanied by a broad polaronic absorption band extending well into the IR region. The polaronic absorption reaches a maximum at V_{GS} = −0.3 V, followed by a decrease in the polaronic absorption while the ground state further bleaches slightly at more negative potentials. This is attributed to increased bipolaron formation at more oxidative potentials, as recently shown for P($g_4$2T-T).[34,35]

Unlike P($g_4$2T-T), the bleaching of BBL ground state absorption does not have the same shape as the pristine ground state absorption shown in Figure S9 (Supporting Information). This is due to overlapping positive polaronic absorption bands, indicating that the fraction of polaronic BBL cannot be directly derived from the amplitude of the ground state bleach. In addition, BBL has multiple positive polaronic absorption bands with maxima at 400, 720, and 865 nm. The 720 and 865 nm bands are close to each other in energy and form one broad absorption band at the largest applied gate voltages. This band reaches a magnitude that is a third in intensity of the pristine ground state absorption, which is more intense than previously published spectra of molecularly doped BBL films.[33] We can conclusively say that the bulk of both P($g_4$2T-T) and BBL are extensively doped under operating conditions, contrasting to what would be expected if the materials were operating in a field effect regime, where only a thin layer at the polymer surface forms a conductive path.

© 2021 The Authors. Advanced Electronic Materials published by Wiley-VCH GmbH

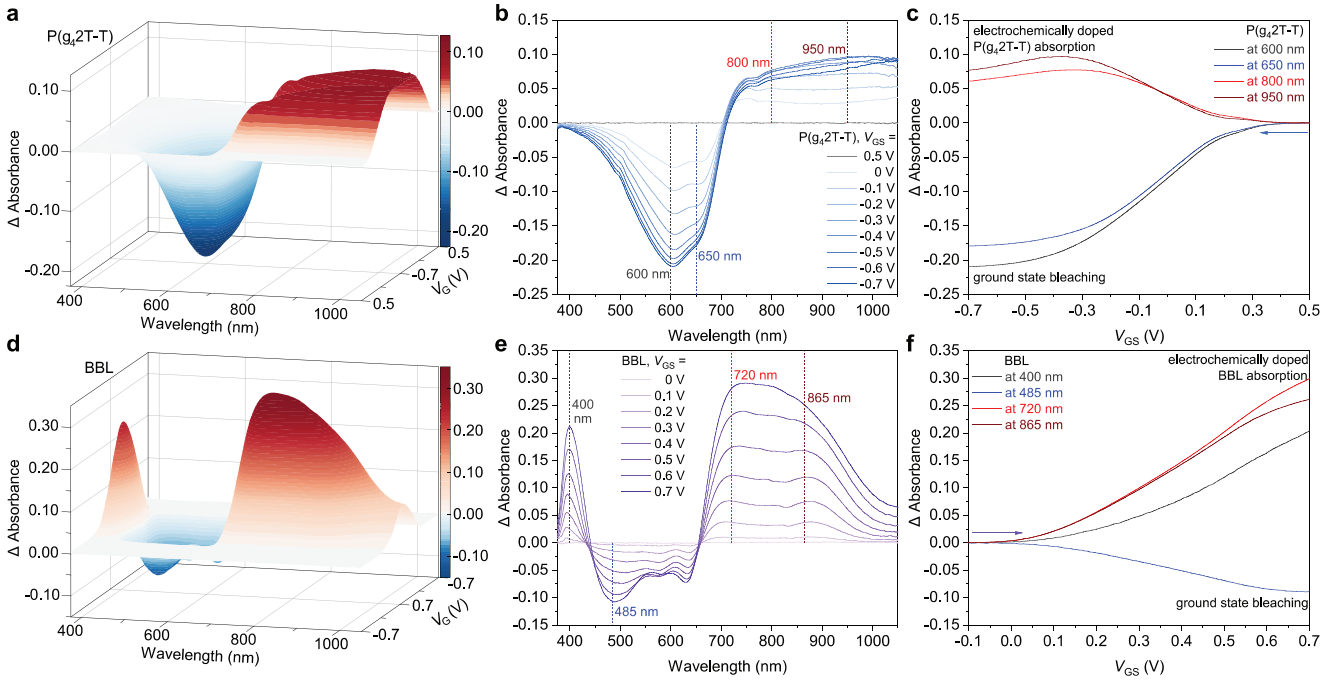

Figure 3. a) Differential absorption spectra of P(g42T-T) scanned between 0.5 and –0.7 V versus Ag/AgCl. b) Differential absorption spectra of P(g42T-T) at select voltages during the negative CV scan. c) Differential absorbance of P(g42T-T) at select wavelengths during the negative CV scan. d) Differential absorption spectra of BBL scanned between –0.7 and 0.7 V versus Ag/AgCl. e) Differential absorption spectra of BBL at select voltages during the positive CV scan. f) Differential absorbance of BBL at select wavelengths during the positive CV scan. All the absorption values are reported as difference absorbance from the undoped state, the voltage scan rate is 50 mV s^{-1}.

2.4. Printed OECT-Based Complementary Inverters

Having validated a pair of well-balanced p-type and n-type OECTs working in enhancement-mode, we demonstrate a printed complementary inverter that yields large gains (≈26 V/V) at a low supply voltage (<0.7 V). The schematic of an OECT-based complementary inverter is shown in **Figure 4**a where P($g_4$2T-T) and BBL OECTs are switched either ON or OFF depending on the input voltage V_{in} at the gate, resulting in a V_{out} which is either equal to V_{DD} (ON, p-type doped, n-type dedoped) or to the ground (OFF, n-type doped, p-type dedoped). To make the transistors switch properly, their V_T play an important role. The low V_T for both P($g_4$2T-T) and BBL OECTs enables the low voltage operation of the printed complementary inverter.

The switching threshold of an inverter (V_M), defined as when V_{in} equals V_{out}, is an indication of the balanced driving strengths of p-type and n-type transistors, and ideally, the threshold is equal to $V_{DD}/2$. The switching threshold is shown in Figure 4b, and it closely follows the ideal behaviors at all V_{DD}. Another benefit of balanced p-type and n-type OECTs is to obtain large high and low noise margins (NM_H and NM_L), defined as follows:

$$NM_H = V_{DD} - V_{IH},\ NM_L = V_{IL} \tag{3}$$

where V_{IH} and V_{IL} are the input voltages HIGH and LOW at the operation points of $\frac{\partial V_{out}}{\partial V_{in}} = -1$ at the voltage transfer characteristics (VTC) of the inverter (Figure 4b). Here, the NM_H and NM_L are listed in Table S1 (Supporting Information) and the total NM with respect to V_{DD} is up to 89% (V_{DD} = 0.7 V).

The voltage gain A_v in units of V/V and decibels (dB) is defined as:

$$A_V = \left|\frac{\partial V_{out}}{\partial V_{in}}\right| \quad (\mathrm{V/V}), A_V = 20log\left|\frac{\partial V_{out}}{\partial V_{in}}\right| \quad (\mathrm{dB}) \tag{4}$$

As shown in Figure 4c, the maximum gain reaches 26 V/V at V_{DD} = 0.7 V, and a relatively high gain of 7.5 V/V can be obtained even with a very low supply voltage of 0.3 V. When V_{DD} is further reduced to 0.2 V, a major deterioration in the VTC is observed with a greatly reduced gain of 2.7 V/V. This is due to the supply voltage approaching the threshold voltage limit. For comparison, unipolar inverters composed of the same printed OECTs (either n-type or p-type only) show maximum gain lower than 1.8 V/V even for V_{DD} of 0.7 V (Figures S10 and S11, Supporting Information).

Low power consumption is another major advantage of CMOS-like technologies since one of the two transistors is always in the nonconducting OFF-state in static conditions. The current at V_{DD} = 0.7 V is below 17 nA, yielding a static power consumption of only 12 nW, which is far lower than that of state-of-the-art unipolar OECT-based inverters (1.18 mW).[8] Even during the switching of the inverter, the maximum power consumption per logic gate is just 2.7 µW, and reaches only 0.10 µW at lower supply voltage (0.3 V). For comparison, previous attempts to develop complementary OECT-based inverters[25,26] yielded a maximum power consumption of 10–15 µW and a static power consumption of 1.35 µW at V_{DD} = 0.6 V. If implemented in fully

© 2021 The Authors. Advanced Electronic Materials published by Wiley-VCH GmbH

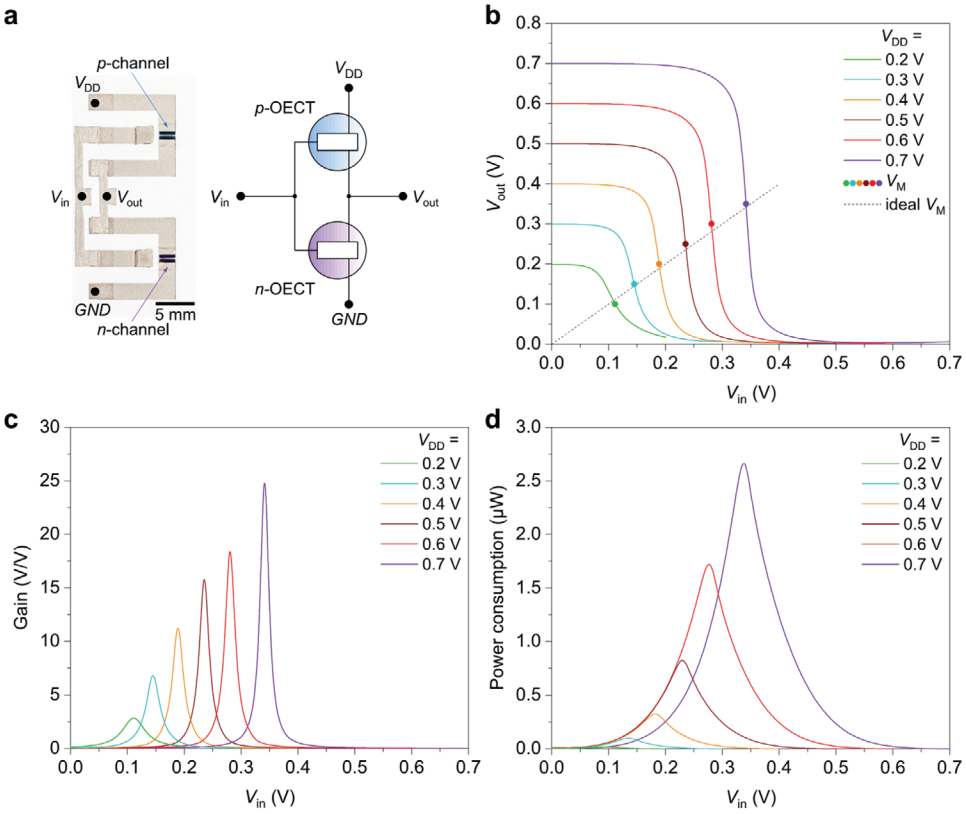

Figure 4. a) Photograph and schematic of a printed complementary inverter. b) Typical voltage transfer characteristics (VTC) of the printed inverter at various supply voltages (0.7–0.2 V). c) Voltage gain of the inverter at various supply voltages. d) Power consumption of the inverter at various supply voltages.

printed large-scale digital circuits, such as a 4-to-7 decoder and 7-bit shift register,[8] the complementary OECTs presented in this work could enable a power consumption reduction of up to 99.8%.

In order to thoroughly evaluate the performance of the inverters, a five-stage ring oscillator, the largest circuit based on complementary OECTs in terms of the number of OECTs, was implemented by cascading five inverters (Figures S12 and S13, Supporting Information). This OECT-based ring oscillator shows a stable oscillation with a period of 6.9 s which gives a stage delay of 690 ms by $t = 1/(2Nf)$, where f is the oscillation frequency and N is the number of stages. The stage delay is consistent with the switching characteristics of the individual OECTs and shows the true operation speed in multistage circuitries. The successful implementation of 10 complementary OECTs into a fully functional five-stage ring oscillator shows potential for large-scale integration.

2.5. Printed OECT-Based Push-Pull Voltage Amplifiers

Although typically implemented as digital devices, CMOS inverters can be used as analog amplifiers. A major advantage of using CMOS inverters as amplifiers in the push-pull configuration (**Figure 5**a), as opposed to active load and/or current source load configurations, is that these devices benefit from the summation of the transconductance of both transistors,[29] as shown in Equation (5). The voltage gain of an OECT-based CMOS-like inverter can be calculated as:

$$A_V = -\left(g_{mp} + g_{mn}\right)\left(r_{op} // r_{on}\right) \tag{5}$$

where g_{mp} and g_{mn} are the transconductances and r_{op} and r_{on} are output resistances of the p-type and n-type transistors, respectively. The main challenge in operating OECT-based CMOS-like inverters is to correctly bias the inverter to position the operation point in the transition region (close to the switching threshold V_M), where both transistors work in the saturation region and the inverter exhibits a large gain. Our push-pull amplifiers with printed complementary OECTs show a gain of 16 (V/V) (24 dB) when amplifying a 10 mV (amplitude) sinusoidal signal with a DC offset of 0.28 V (Figure 5b), which is consistent with the DC gain of the inverter shown in Figure 4c. When amplifying signals as low as 100 μV, the voltage gain reaches 29 (V/V) (29.2 dB), as shown in Figures S14 and S15 (Supporting Information). The maximum amplification observed is 33 (V/V) (30.4 dB) with a 200 μV input signal (Figure 5c). We evaluated the gain of the voltage amplifier with respect to input frequencies ranging from 0.06 to 5 Hz with a 10-mV input signal. The detailed waveforms at each frequency are shown in Figures S14 and S15 (Supporting Information).

These OECT-based single stage push-pull amplifier can serve as a building block for more complex amplifiers. Here, we demonstrate a monolithically integrated two-stage amplifier to

© 2021 The Authors. Advanced Electronic Materials published by Wiley-VCH GmbH

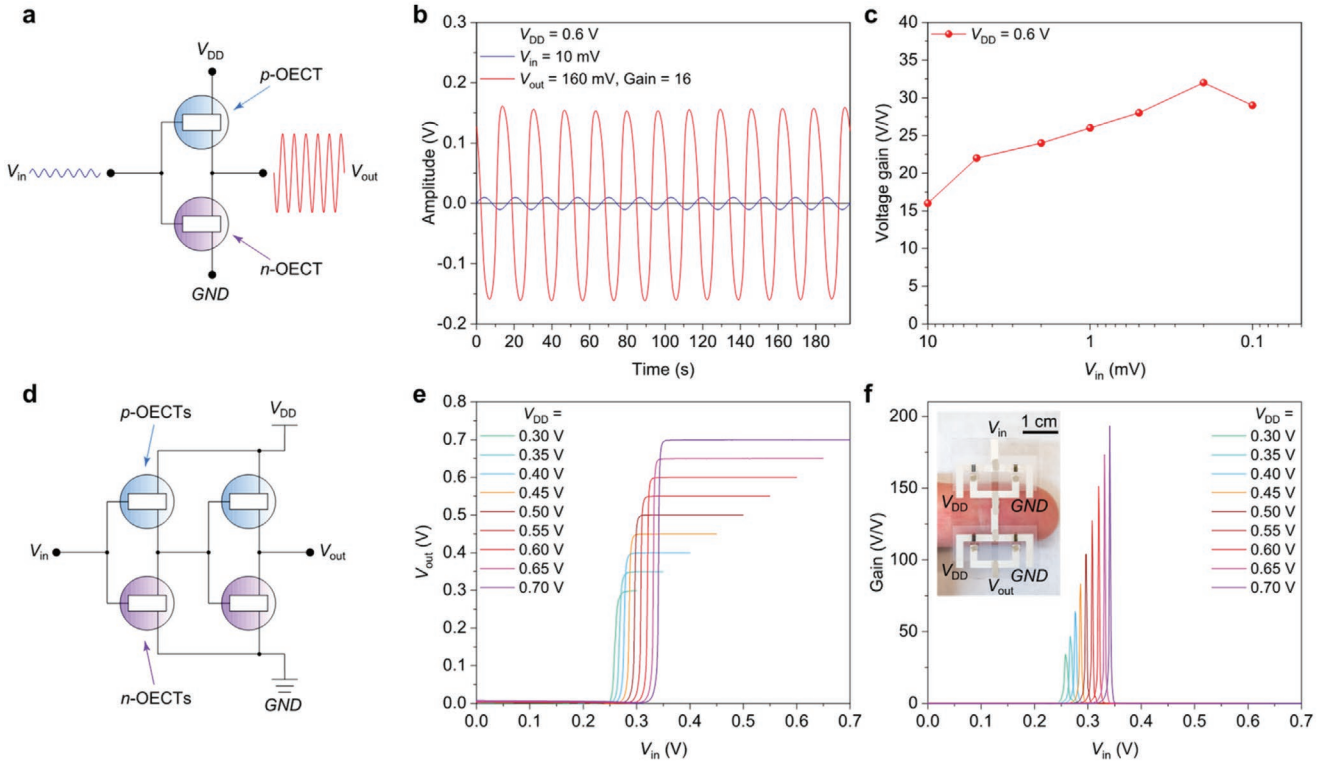

Figure 5. a) Illustration of the amplifier configuration used to obtain these measurements. b) Voltage waveform of input and output signals when a 10 mV and 0.06 Hz sinusoid voltage is applied as the input. c) Voltage gain dependence on the amplitude of the input signals (10 mV–100 µV). d) Schematic of a five-stage push-pull CMOS amplifier. e) Voltage transfer characteristics (VTC) of a two-stage amplifier. f) Voltage gain of a two-stage amplifier. Inset, photograph of the monolithically integrated two-stage amplifier.

obtain a high voltage gain by cascading two single-stage amplifiers, as shown in Figure 5d. Matching the operating point is crucial for the successful integration of the two single-stage amplifiers. For both stages, the operation points are optimized at V_M which is close to the ideal value in our complementary OECT inverters. The two-stage amplifier exhibits a voltage gain as high as 193 (V/V), which is the highest reported for OECT-based amplifiers. For comparison, the highest voltage gain among OECT technologies reported to date is 107 (V/V) for depletion-mode, p-type PEDOT:PSS-based OECTs. These unipolar OECTs however require a supply voltage of 0.8 V and consume ≈480 µW of power.[25] Here, we are able to almost double the voltage amplification while reducing the maximum power consumption (5.6 µW) by close to 99%.

By coupling the printed enhancement-mode OECTs operated at low voltage and the complementary push-pull configuration, we are able to demonstrate flexible voltage amplifiers with high gain and very low power dissipation. In order to evaluate the amplifier performance with respect to power efficiency, we normalize the voltage gain to the maximum power consumption at various supply voltages using the equation $A_{V/P} = A_V/P_{max}$ (dB µW^{-1}). Here, the normalized voltage gain $A_{V/P}$ for the printed voltage amplifiers (single stage) reaches 10.2 dB µW^{-1} at V_{DD} = 0.7 V and 169 dB µW^{-1} at V_{DD} = 0.3 V, which is up to 50 times higher than that of state-of-the-art OECT amplifiers[23–25] (Table S2, Supporting Information). In addition to existing OECT technologies, we have also compared our results with inverters based on electrolyte-gated thin-film transistors[36–39] and recently reported voltage amplifiers with organic field-effect transistors.[40–44] Cutting-edge voltage amplifiers, that implement unipolar organic field-effect transistors in differential[44] and pseudo-CMOS[43] circuit configurations and are typically operated at a few volts, reach normalized gain values of 5 dB µW^{-1} (differential) and 4.6 dB µW^{-1} (pseudo-CMOS). Electrolyte-gated thin-film transistors (e.g., IGZO,[38] CNT[39]) are usually operated at around 1 V and their inverters generally exhibit normalized gains between 0.03 and 0.75 dB µW^{-1}. From the comparison, we can see that complementary OECT-based amplifiers offer a power-efficient solution to sense weak voltage signals (as low as 100 µV) at low supply voltages (as low as 0.3 V). Power efficiency is crucial for self-powered applications[45] where the power supply is heavily limited. For example, commercially available printed, flexible organic solar cells can yield about 18 µW cm^{-2} with indoor lighting.[46] Thermoelectric generators typically offer a few microvolts with a maximum of 28.5 µW cm^{-2} for a temperature difference of 10 °C.[47] Electrostatic generators can provide around 50 µW cm^{-2},[48] while electromagnetic generators can supply up to 150 µW cm^{-2}.[49] This shows that our printed voltage amplifier has huge potential for self-powered devices.

As we demonstrated, the voltage gain of the printed amplifier can be further increased by cascading multiple stages together. With two-stage printed amplifiers, we report DC gain of 193 V/V, which, to the best of our knowledge, is the highest among the OECT technologies[25,26] and also among the best for sub-1V amplifiers based on emerging CMOS-like

© 2021 The Authors. Advanced Electronic Materials published by Wiley-VCH GmbH

technologies such as vacuum-processed small-molecule-based OFETs,[50] CNTs,[51,52] graphene,[53] and 2D transition metal dichalcogenide[54–59] (see Table S3, Supporting Information). As an example, a hybrid CMOS-like inverter based on CNT and quantum dots transistors operates with a DC gain of 76 V/V at V_{DD} = 0.9 V, while the highest gain among 2D transition metal dichalcogenide transistors (p-type WSe2 and n-type MoS2) is 34 V/V at V_{DD} = 1 V. Furthermore, our printed complementary OECT circuits exhibit excellent flexibility, with no sign of degradation upon 10 bending cycles at a radius of 4 mm (Figure S16, Supporting Information).

3. Conclusions

We have developed flexible, printed digital, and analog circuits composed of complementary p-/n-type enhancement mode OECTs. The p- and n-type OECTs incorporate P($g_4$2T-T) and BBL as the channel material, and polycationic PQ-10 and polyanionic PSSNa hydrogels as the electrolyte, respectively. Planarly integrated side-gate configuration of screen-printed OECTs enables large-scale integration of complementary circuits in a cost-efficient manner. By engineering the thickness of the active materials, we match the driving strengths of the p-type and n-type OECTs with identical channel dimensions. Both types of OECTs exhibit low V_T (–0.22 V for P(g42T-T) OECTs and 0.16 V for BBL OECTs), which enables the single-stage amplifier to operate at a low voltage and with a power-normalized gain of up to 169 dB μW^{-1}, which is 53 times higher than current state-of-the-art OECT amplifiers. In addition, the single-stage amplifier is able to sense very low amplitude signals, as low as 100 µV, with a maximum gain of 30.4 dB. Furthermore, the monolithically integrated two-stage amplifier reaches a DC gain of 193 V/V, which is a record-high value among all emerging sub-1V CMOS-like technologies.

With such a high power efficiency, we envisage that our flexible and fully printable OECT-based voltage amplifiers may find several applications in recording/monitoring of weak voltage signals, such as IoT sensing, electrophysiological, and other bioelectric infra-slow signals,[60,61] with limited availability to power supply or a need for on-site amplification. To further extend the amplifiers' operating frequency range, one could improve the OECT switching speed by, e.g., scaling down the device geometry[62] and/or engineering the channel semiconductor.[62,63] The progress of electrophysiological signal recordings and electronic neural interfaces has been tending toward autonomous, implantable, wearable devices integrated with sensing electrodes, and signal processing units.[64] Long-term wireless monitoring on a mobile curvilinear surface requires flexible and power-efficient amplifiers that operate at low voltages and draw little current to extend the limits imposed by battery capacity. To summarize, our printed complementary voltage amplifiers may address many key challenges posed in the wireless detection of weak sensor signals by demonstrating the potentials of a) in situ pre-amplification of small signals, b) flexibility for conformable/wearable electronics, c) low power consumption for implants, d) scalability for massively parallel recording by screen-printing manufacturing, e) electrolyte nature at the input (gates of OECTs) for good interface to skin and organs, and f) potential signal filtering and processing with OECT-based circuitries.

4. Experimental Section

Materials: The polyethylene terephtalate (PET) substrate Polifoil Bias was purchased from Policrom Screen. Silver ink (Ag 5000, DuPont) was used for printed interconnects. Carbon ink 7102 printing paste (DuPont) was used for drain/source/gate contacts. Insulating ink (5018, DuPont) was used for electrode isolation. PQ-10, PSSNa, and BBL were purchased from Sigma-Aldrich and used as received. P($g_4$2T-T) was synthesized following the procedure reported previously (M_n = 24 kDa, polydispersity index = 3.3).[65]

Sample Preparation: The P($g_4$2T-T) and BBL inks were fabricated through a surfactant-free method. P($g_4$2T-T) (30 mg) was dissolved in chloroform (15 mL) to form a dark magenta solution, then the P($g_4$2T-T)-chloroform solution was dropwise added to IPA (75 mL) under high-speed stirring (1500 rpm). During the solvent-exchange, bright blue nanoparticles were generated. BBL (30 mg) was dissolved in MSA (15 mL) to form a deep red solution, then the BBL-MSA solution was dropwise added to IPA (75 mL) under high speed stirring (1500 rpm). During the solvent-exchange, dark purple (for BBL) nanoparticles were generated. The P($g_4$2T-T) and BBL nanoparticles were, respectively, collected by centrifugation (5000 rpm, 30 min) and washed by IPA for 6 times until neutral. The neutral P($g_4$2T-T) and BBL nanoparticles were re-dispersed in IPA to obtain a dispersion ink (about 0.006 mg mL^{-1} for P($g_4$2T-T) and 0.1 mg mL^{-1} for BBL). The preparation of the electrolyte hydrogels was done as follows. PQ-10 (2.5 g) was added to water (7.5 mL) in a 20 mL reaction vessel and was then sealed and stirred at 150 °C for 4 h until a uniform, bubble-free highly viscous hydrogel was formed. The PQ-10 hydrogel was then cooled down to room temperature before use. PSSNa (4.0 g), *d*-sorbitol (1.0 g), and glycerol (1.0 g) were added to water (4.0 mL) in a 20 mL reaction vessel and the mixer was sealed and stirred at 150 °C for 4 h until a uniform, bubble-free highly viscous hydrogel was formed. The PSSNa hydrogel was then cooled down to room temperature before use.

Fabrication of OECTs and Inverters/Amplifiers: All materials were deposited by flatbed sheet-fed screen-printing equipment (DEK Horizon 03iX) on top of PET plastic substrates (Figure S3a, Supporting Information). The printed features of the design layout covered approximately the area of an A4 sheet. A layer of carbon was first deposited on the substrate by screen-printing to form the contacts. Ag 5000 silver ink was then patterned by screen-printing, followed by an insulating layer of 5018 ink patterned by screen-printing, which was UV-cured to define the area of the gate and channel. Ag/AgCl gate layer was fabricated by spray-coating in air using Ag/AgCl ink through a shadow mask, by means of a standard HD-130 airbrush (0.3 mm) with atomization air pressure of 1 bar, then annealed at 100 °C for 2 min. The P($g_4$2T-T) and BBL layer were fabricated by spray-coating in air through a shadow mask. The PQ-10 or PSSNa hydrogel electrolyte layer was fabricated by screen-printing.

Spectroelectrochemistry: Absorption measurements were performed on BBL and P($g_4$2T-T) electrodes on FTO glass using an AvaSpec ULS2048L fiber optic spectrometer and an AvaLight HAL-S-Mini light source (Avantes BV). The electrode was immersed in 0.1 M NaCl solution inside a three-electrode electrochemical cell with a platinum wire counter electrode and a Ag/AgCl reference electrode. CV scans were performed with a potentiostat (BioLogic SP-200). The electrodes were first fully dedoped by applying a potential of –0.7 V for BBL and 0.5 V for P($g_4$2T-T) for 10 s, during which time the absorption baseline was measured, followed by running a CV scan between –0.7 and 0.7 V for BBL and between 0.5 and –0.7 V for P($g_4$2T-T) to match with the gate voltage range applied to the transistors. The scan speed was 50 mV s^{-1}. The potentiostat triggered the absorption measurement to begin at the exact same time as the CV scan, with averages of 8 absorption spectra saved every 10 ms.

© 2021 The Authors. Advanced Electronic Materials published by Wiley-VCH GmbH

Morphology Characterization: Atomic force microscopy (AFM) was performed with a Dimension 3100/Nanoscope IV system operating in tapping mode. Si tips having a force constant of 40 N m^{-1} were used to record the topographies.

Characterization of OECTs and Amplifiers: All measurements are performed in ambient at a temperature of ≈20 °C and at a relative humidity of ≈45%. Transfer and dynamic switch measurements were performed by using a semiconductor parameter analyzer (Keithley 4200 SCS) and a probe station.

Supporting Information

Supporting Information is available from the Wiley Online Library or from the author.

Acknowledgements

The authors thank Robert Forchheimer (Linköping U.), Kai Xu (Yanshan U.), Hengda Sun (Donghua U.), Mary Donahue (Linköping U.), and Silan Zhang (Linköping U.) for helpful discussion. The authors also thank Robert Brooke, Marie Nilsson, and Jan Strandberg (RISE) for assistance with screen-printing the electrodes. This work was financially supported by the Knut and Alice Wallenberg foundation, the Swedish Research Council (2016-03979 and 2020–03243), Swedish Foundation for Strategic Research (SE13-0045), ÅForsk (18-313 and 19–310), Olle Engkvists Stiftelse (204-0256), VINNOVA (2020-05223), the European Commission through the FET-OPEN project MITICS (GA-964677), and the Swedish Government Strategic Research Area in Materials Science on Functional Materials at Linköping University (Faculty Grant SFO-Mat-LiU 2009-00971).

Conflict of Interest

The authors declare no conflict of interest.

Data Availability Statement

The data that support the findings of this study are available from the corresponding author upon reasonable request.

Keywords

organic electrochemical transistors, organic mixed ion-electron conductors, screen-printing, voltage amplifiers

Received: August 30, 2021
Revised: November 10, 2021
Published online:

[1] R. H. Dennard, F. H. Gaensslen, H. N. Yu, V. L. Rideout, E. Bassous, A. R. Leblanc, *IEEE J. Solid-State Circuits* **1974**, *9*, 256.
[2] T. Hiramoto, *Nat. Electron.* **2019**, *2*, 557.
[3] D. De Donno, L. Catarinucci, L. Tarricone, *IEEE Trans. Instrum. Meas.* **2014**, *63*, 1701.
[4] B. D. Paulsen, K. Tybrandt, E. Stavrinidou, J. Rivnay, *Nat. Mater.* **2020**, *19*, 13.
[5] B. D. Paulsen, S. Fabiano, J. Rivnay, *Annu. Rev. Mater. Res.* **2021**, *51*, 73.
[6] J. Rivnay, S. Inal, A. Salleo, R. M. Owens, M. Berggren, G. G. Malliaras, *Nat. Rev. Mater.* **2018**, *3*, 17086.
[7] D. Tu, S. Fabiano, *Appl. Phys. Lett.* **2020**, *117*, 080501.
[8] P. Andersson Ersman, R. Lassnig, J. Strandberg, D. Tu, V. Keshmiri, R. Forchheimer, S. Fabiano, G. Gustafsson, M. Berggren, *Nat. Commun.* **2019**, *10*, 5053.
[9] P. Andersson Ersman, D. Westerberg, D. Tu, M. Nilsson, J. Åhlin, A. Eveborn, A. Lagerlöf, D. Nilsson, M. Sandberg, P. Norberg, M. Berggren, R. Forchheimer, G. Gustafsson, *Flexible Printed Electron.* **2017**, *2*, 045008.
[10] P. C. Hutter, T. Rothlander, G. Scheipl, B. Stadlober, *IEEE Trans. Electron Devices* **2015**, *62*, 4231.
[11] C. Y. Yang, M. A. Stoeckel, T. P. Ruoko, H. Y. Wu, X. Liu, N. B. Kolhe, Z. Wu, Y. Puttisong, C. Musumeci, M. Massetti, H. Sun, K. Xu, D. Tu, W. M. Chen, H. Y. Woo, M. Fahlman, S. A. Jenekhe, M. Berggren, S. Fabiano, *Nat. Commun.* **2021**, *12*, 2354.
[12] T. Someya, Z. Bao, G. G. Malliaras, *Nature* **2016**, *540*, 379.
[13] M. Berggren, A. Richter-Dahlfors, *Adv. Mater.* **2007**, *19*, 3201.
[14] D. T. Simon, E. O. Gabrielsson, K. Tybrandt, M. Berggren, *Chem. Rev.* **2016**, *116*, 13009.
[15] J. Y. Gerasimov, R. Gabrielsson, R. Forchheimer, E. Stavrinidou, D. T. Simon, M. Berggren, S. Fabiano, *Adv. Sci.* **2019**, *6*, 1801339.
[16] J. Y. Gerasimov, D. Zhao, A. Sultana, T. Abrahamsson, S. Han, D. Bliman, D. Tu, D. T. Simon, R. Olsson, X. Crispin, M. Berggren, S. Fabiano, *Adv. Electron. Mater.* **2021**, *7*, 2001126.
[17] E. J. Fuller, S. T. Keene, A. Melianas, Z. Wang, S. Agarwal, Y. Li, Y. Tuchman, C. D. James, M. J. Marinella, J. J. Yang, A. Salleo, A. A. Talin, *Science* **2019**, *364*, 570.
[18] M. Giordani, M. Sensi, M. Berto, M. Di Lauro, C. A. Bortolotti, H. L. Gomes, M. Zoli, F. Zerbetto, L. Fadiga, F. Biscarini, *Adv. Funct. Mater.* **2020**, *30*, 2002141.
[19] P. Gkoupidenis, D. A. Koutsouras, G. G. Malliaras, *Nat. Commun.* **2017**, *8*, 15448.
[20] P. O. Svensson, D. Nilsson, R. Forchheimer, M. Berggren, *Appl. Phys. Lett.* **2008**, *93*, 203301.
[21] J. Rivnay, P. Leleux, M. Sessolo, D. Khodagholy, T. Hervé, M. Fiocchi, G. G. Malliaras, *Adv. Mater.* **2013**, *25*, 7010.
[22] M. Braendlein, T. Lonjaret, P. Leleux, J.-M. Badier, G. G. Malliaras, *Adv. Sci.* **2017**, *4*, 1600247.
[23] V. Venkatraman, J. T. Friedlein, A. Giovannitti, I. P. Maria, I. McCulloch, R. R. McLeod, J. Rivnay, *Adv. Sci.* **2018**, *5*, 1800453.
[24] P. Romele, M. Ghittorelli, Z. M. Kovács-Vajna, F. Torricelli, *Nat. Commun.* **2019**, *10*, 3044.
[25] P. Romele, P. Gkoupidenis, D. A. Koutsouras, K. Lieberth, Z. M. Kovács-Vajna, P. W. M. Blom, F. Torricelli, *Nat. Commun.* **2020**, *11*, 3743.
[26] H. Sun, M. Vagin, S. Wang, X. Crispin, R. Forchheimer, M. Berggren, S. Fabiano, *Adv. Mater.* **2018**, *30*, 1704916.
[27] S. Lee, A. Nathan, *Science* **2016**, *354*, 302.
[28] C. Jiang, H. W. Choi, X. Cheng, H. Ma, D. Hasko, A. Nathan, *Science* **2019**, *363*, 719.
[29] S. M. Sharroush, *Int. J. Circuit Theory Appl.* **2019**, *47*, 1006.
[30] P. A. Ersman, M. Zabihipour, D. Tu, R. Lassnig, J. Strandberg, J. Åhlin, M. Nilsson, D. Westerberg, G. Gustafsson, M. Berggren, R. Forchheimer, S. Fabiano, *Flexible Printed Electron.* **2020**, *5*, 024001.
[31] B. Schmatz, A. W. Lang, J. R. Reynolds, *Adv. Funct. Mater.* **2019**, *29*, 1905266.
[32] S. T. Keene, T. P. A. Pol, D. Zakhidov, C. H. L. Weijtens, R. A. J. Janssen, A. Salleo, Y. Burgt, *Adv. Mater.* **2020**, *32*, 2000270.
[33] K. Xu, H. Sun, T. P. Ruoko, G. Wang, R. Kroon, N. B. Kolhe, Y. Puttisong, X. Liu, D. Fazzi, K. Shibata, C. Y. Yang, N. Sun, G. Persson, A. B. Yankovich, E. Olsson, H. Yoshida, W. M. Chen, M. Fahlman, M. Kemerink, S. A. Jenekhe, C. Müller, M. Berggren, S. Fabiano, *Nat. Mater.* **2020**, *19*, 738.

© 2021 The Authors. Advanced Electronic Materials published by Wiley-VCH GmbH

[34] I. Sahalianov, J. Hynynen, S. Barlow, S. R. Marder, C. Müller, I. Zozoulenko, *J. Phys. Chem. B* **2020**, *124*, 11280.
[35] S. Zokaei, R. Kroon, J. Gladisch, B. D. Paulsen, W. Sohn, A. I. Hofmann, G. Persson, A. Stamm, P. Syrén, E. Olsson, J. Rivnay, E. Stavrinidou, A. Lund, C. Müller, *Adv. Sci.* **2021**, *8*, 2002778.
[36] Y. Xia, W. Zhang, M. Ha, J. H. Cho, M. J. Renn, C. H. Kim, C. D. Frisbie, *Adv. Funct. Mater.* **2010**, *20*, 587.
[37] K. G. Cho, H. J. Kim, H. M. Yang, K. H. Seol, S. J. Lee, K. H. Lee, *ACS Appl. Mater. Interfaces* **2018**, *10*, 40672.
[38] S. Park, S. Lee, C. H. Kim, I. Lee, W. J. Lee, S. Kim, B. G. Lee, J. H. Jang, M. H. Yoon, *Sci. Rep.* **2015**, *5*, 13088.
[39] M. Ha, J.-W. T. Seo, P. L. Prabhumirashi, W. Zhang, M. L. Geier, M. J. Renn, C. H. Kim, M. C. Hersam, C. D. Frisbie, *Nano Lett.* **2013**, *13*, 954.
[40] M. Guerin, A. Daami, S. Jacob, E. Bergeret, E. Bènevent, P. Pannier, R. Coppard, *IEEE Trans. Electron Devices* **2011**, *58*, 3587.
[41] H. Marien, M. S. J. Steyaert, E. Van Veenendaal, P. Heremans, *IEEE J. Solid-State Circuits* **2011**, *46*, 276.
[42] K. Fukuda, Y. Takeda, Y. Yoshimura, R. Shiwaku, L. T. Tran, T. Sekine, M. Mizukami, D. Kumaki, S. Tokito, *Nat. Commun.* **2014**, *5*, 4147.
[43] T. Sekitani, T. Yokota, K. Kuribara, M. Kaltenbrunner, T. Fukushima, Y. Inoue, M. Sekino, T. Isoyama, Y. Abe, H. Onodera, T. Someya, *Nat. Commun.* **2016**, *7*, 11425.
[44] M. Sugiyama, T. Uemura, M. Kondo, M. Akiyama, N. Namba, S. Yoshimoto, Y. Noda, T. Araki, T. Sekitani, *Nat. Electron.* **2019**, *2*, 351.
[45] S. Park, S. W. Heo, W. Lee, D. Inoue, Z. Jiang, K. Yu, H. Jinno, D. Hashizume, M. Sekino, T. Yokota, K. Fukuda, K. Tajima, T. Someya, *Nature* **2018**, *561*, 516.
[46] epishine, https://www.epishine.com
[47] A. B. Amar, A. B. Kouki, H. Cao, *Sensors* **2015**, *15*, 28889.
[48] R. Tashiro, N. Kabei, K. Katayama, F. Tsuboi, K. Tsuchiya, *J. Artif. Organs* **2002**, *5*, 239.
[49] R. Amirtharajah, A. P. Chandrakasan, *IEEE J. Solid-State Circuits* **1998**, *33*, 687.
[50] U. Zschieschang, V. P. Bader, H. Klauk, *Org. Electron.* **2017**, *49*, 179.
[51] S. Joshi, V. D. Bhatt, E. Jaworska, A. Michalska, K. Maksymiuk, M. Becherer, A. Gagliardi, P. Lugli, *Sci. Rep.* **2018**, *8*, 11386.
[52] A. G. Shulga, V. Derenskyi, J. M. Salazar-Rios, D. N. Dirin, M. Fritsch, M. V. Kovalenko, U. Scherf, M. A. Loi, *Adv. Mater.* **2017**, *29*, 1701764.
[53] A. Dathbun, S. Kim, S. Lee, D. K. Hwang, J. H. Cho, *Mol. Syst. Des. Eng.* **2019**, *4*, 484.
[54] M. H. Alam, Z. Xu, S. Chowdhury, Z. Jiang, D. Taneja, S. K. Banerjee, K. Lai, M. H. Braga, D. Akinwande, *Nat. Commun.* **2020**, *11*, 3203.
[55] A. Pezeshki, S. H. Hosseini Shokouh, P. J. Jeon, I. Shackery, J. S. Kim, I. K. Oh, S. C. Jun, H. Kim, S. Im, *ACS Nano* **2016**, *10*, 1118.
[56] J. Y. Lim, A. Pezeshki, S. Oh, J. S. Kim, Y. T. Lee, S. Yu, D. K. Hwang, G.-H. Lee, H. J. Choi, S. Im, *Adv. Mater.* **2017**, *29*, 1701798.
[57] Y. W. Lan, P. C. Chen, Y. Y. Lin, M. Y. Li, L. J. Li, Y. L. Tu, F. L. Yang, M. C. Chen, K. S. Li, *Nanoscale Horiz.* **2019**, *4*, 683.
[58] M. Tosun, S. Chuang, H. Fang, A. B. Sachid, M. Hettick, Y. Lin, Y. Zeng, A. Javey, *ACS Nano* **2014**, *8*, 4948.
[59] S. Larentis, B. Fallahazad, H. C. P. Movva, K. Kim, A. Rai, T. Taniguchi, K. Watanabe, S. K. Banerjee, E. Tutuc, *ACS Nano* **2017**, *11*, 4832.
[60] Z. I. Lázár, D. J. Dijk, A. S. Lázár, *J. Neurosci. Methods* **2019**, *316*, 22.
[61] E. Masvidal-Codina, X. Illa, M. Dasilva, A. B. Calia, T. Dragojević, E. E. Vidal-Rosas, E. Prats-Alfonso, J. Martínez-Aguilar, J. M. De la Cruz, R. Garcia-Cortadella, P. Godignon, G. Rius, A. Camassa, E. Del Corro, J. Bousquet, C. Hébert, T. Durduran, R. Villa, M. V. Sanchez-Vives, J. A. Garrido, A. Guimerà-Brunet, *Nat. Mater.* **2019**, *18*, 280.
[62] H. Wu, C. Yang, Q. Li, N. B. Kolhe, X. Strakosas, M. Stoeckel, Z. Wu, W. Jin, M. Savvakis, R. Kroon, D. Tu, H. Y. Woo, M. Berggren, S. A. Jenekhe, S. Fabiano, *Adv. Mater.* **2021**, 2106235.
[63] S. Zhang, M. Massetti, T. P. Ruoko, D. Tu, C. Y. Yang, X. Liu, Z. Wu, Y. Lee, R. Kroon, P. O. Å. Persson, H. Y. Woo, M. Berggren, C. Müller, M. Fahlman, S. Fabiano, *Adv. Funct. Mater.* **2021**, 2106447.
[64] M. Zhang, Z. Tang, X. Liu, J. Van der Spiegel, *Nat. Electron.* **2020**, *3*, 191.
[65] R. Kroon, D. Kiefer, D. Stegerer, L. Yu, M. Sommer, C. Müller, *Adv. Mater.* **2017**, *29*, 1700930.

© 2021 The Authors. Advanced Electronic Materials published by Wiley-VCH GmbH